Anomalously High Proton Conduction of Interfacial Water

V.G. Artemov[1*], E. Uykur[2], P.O. Kapralov[3], A. Kiselev[4], K. Stevenson[1], H. Ouerdane[1], M. Dressel[2]

[1] Center for Energy Science and Technology, Skolkovo Institute of Science and Technology, 121205 Moscow, Russia

[2] 1. Physikalisches Institut, Universität Stuttgart, 70569 Stuttgart, Germany

[3] Russian Quantum Center, 143025 Moscow, Russia

[4] Institute of Meteorology and Climate Research, Karlsruhe Institute of Technology, 76021 Karlsruhe, Germany

* e-mail: v.artemov@skoltech.ru

Water at the solid-liquid interface exhibits an anomalous ionic conductivity and dielectric constant compared to bulk water. Both phenomena still lack a detailed understanding. Here, we report radiofrequency measurements and analyses of the electrodynamic properties of interfacial water confined in nano-porous matrices formed by diamond grains of various sizes, ranging from 5 nm to 0.5 μm in diameter. Contrary to bulk water, the charge-carrying protons/holes in interfacial water are not mutually screened allowing for higher mobility in the external electric field. Thus, the protonic conductivity reaches a maximum value, which can be five orders of magnitude higher than that of bulk water. Our results aid in the understanding of physical and chemical properties of water confined in porous materials, and pave the way to the development of new type of highly-efficient proton-conductive materials for applications in electrochemical energy systems, membrane separations science and nano-fluidics.

Pure liquid water is a low-conductive dielectric medium whose ionic conductivity is governed by mobility of its intrinsic ions, H_3O^+ and OH^-. In many natural and artificial systems, such as rocks, polymers, nanostructures and biological cells, water is confined in small volumes limited by the boundary surface and exhibits properties significantly different from that of bulk water. In such conditions, the water layer near the interface boundary often dominates the overall properties of such aqueous system. Low viscosity, low dielectric constant, high molecular mobility, excess charge, free energy and ultrafast processes under irradiation in "interfacial water" have been observed experimentally and studied theoretically[1,2,3,4,5,6,7]. However, the electrodynamics of interfacial water, which governs its structural and dynamical properties at microscopic level, is still poorly understood. In particular, the molecular mechanisms of electrical charge separation responsible for atmospheric electricity[8], pulse propagation in neuronal networks[9], charge transfer and storage[10] must be elucidated. In addition, the technological development of electrochemical energy storage systems including supercapacitors, fuel cells, and batteries is hindered because of the incomplete knowledge of the physical and chemical properties of interfacial water in nano-scale confinement[11,12,13].

The dielectric properties of interfacial water have previously been studied by means of spectroscopy in a broad variety of porous solids[9,14,15,16,17,18]. Different mechanisms, such as ionic conductivity in the chemisorbed/physisorbed water[19], space charge effects due to partial adsorption[20], and correlated near-the-surface-diffusion[6], have been discussed. Nevertheless, because the stoichiometry of the chemical reactions taking place on the walls of the porous matrix is usually unknown, the generalization of the interfacial water properties is problematic. Indeed, both the geometry and the material properties of the confining medium may mask the intrinsic water properties, which are inseparable from the effective media dielectric response. For example, the electrodynamics of confined water appears to be strongly dependent on the type of material, its porosity, tortuosity, pore

size, and surface chemical reactions[21]. Recently, an anomalously low dielectric constant ε of strongly confined water – one order of magnitude lower than for the bulk water – was reported[3]. However, the method used in[3] did not provide a possibility to measure the conductivity σ of interfacial water, and hence the understanding of water electrodynamics remained incomplete. In the present study, we derive the previously not reported intrinsic permittivity $\varepsilon'(\omega)$ and conductivity $\sigma(\omega)$ of interfacial water from the values measured for the effective porous media to obtain the information on the mechanism of the charge transfer along a water-solid interface[22,23].

We used single-crystalline diamond particles of different sizes d of 5, 40, 80, 120, 200 and 500 nanometers, to prepare a radio-frequency-transparent porous matrix (ceramic pellets). All diamond powders were purchased from a single manufacturer (Adámas Nanotechnologies) and produced by the same high pressure-high temperature (HPHT) method with subsequent milling, except for the 5-nm crystals, which were obtained by detonation technique[24]. We filled ceramic pellets channels with water by exposing to saturated water vapor, and applied the broadband dielectric spectroscopy to measure the complex impedance Z^* as shown in Fig. 1a. The samples were placed between two parallel-plate gold electrodes. By applying an AC voltage in the 10^{-1} to 10^7 Hz range, the frequency-dependent capacitance $C_2(\omega)$ and conductance $G(\omega)$ of the sample were obtained in the 0 to 100 °C temperature interval using the equivalent circuit shown in Fig. 1b. The static dielectric constant ε, and DC conductivity σ of the sample were obtained from the $C_2(\omega)$ and $G(\omega)$ spectra using standard formalism[25]. Distinctive features of the diamond: high chemical stability, very low electronic conductivity ($\sigma_d \approx 10^{-10}$ S/cm) and dielectric constant ($\varepsilon_d \approx 6$), allows us to unambiguously unravel the intrinsic electrodynamic parameters of interfacial water.

Figures 1, c to e, displays scanning electron-microscopy images of the diamond powders, which were preliminary cleaned to minimize the concentration of unavoidable contaminants: amorphous carbon,

weakly bound surface groups and metal impurities[24]. The powders were boiled in hydrochloric acid, centrifuged several times in double-distilled water until the pH stabilization was reached, and dried for four hours at 350 °C. The sample purity was characterized by means of infrared spectroscopy, X-rays diffraction, titration, electronic microscopy, and energy-dispersive X-ray analysis, which showed a presence of COOH groups with small concentration about one group per grain, and negligible amount of foreign contaminants on the treated diamond surface. Porosity, pore size distributions and total pore volume of the pressed pellets were determined by gas adsorption analysis (see SI, Figs. s5-s7). We found a narrow distribution of open pores with consistent change of the radius *r* of pores from 2 to 200 nm with the change of grain sizes *d* from 5 to 500 nm. As the grain size decreases, the relative amount of bulk water (shown in light blue in Fig. 1, f to h) is consistently decreasing, and finally approaching the limit of interfacial water (shown in deep blue).

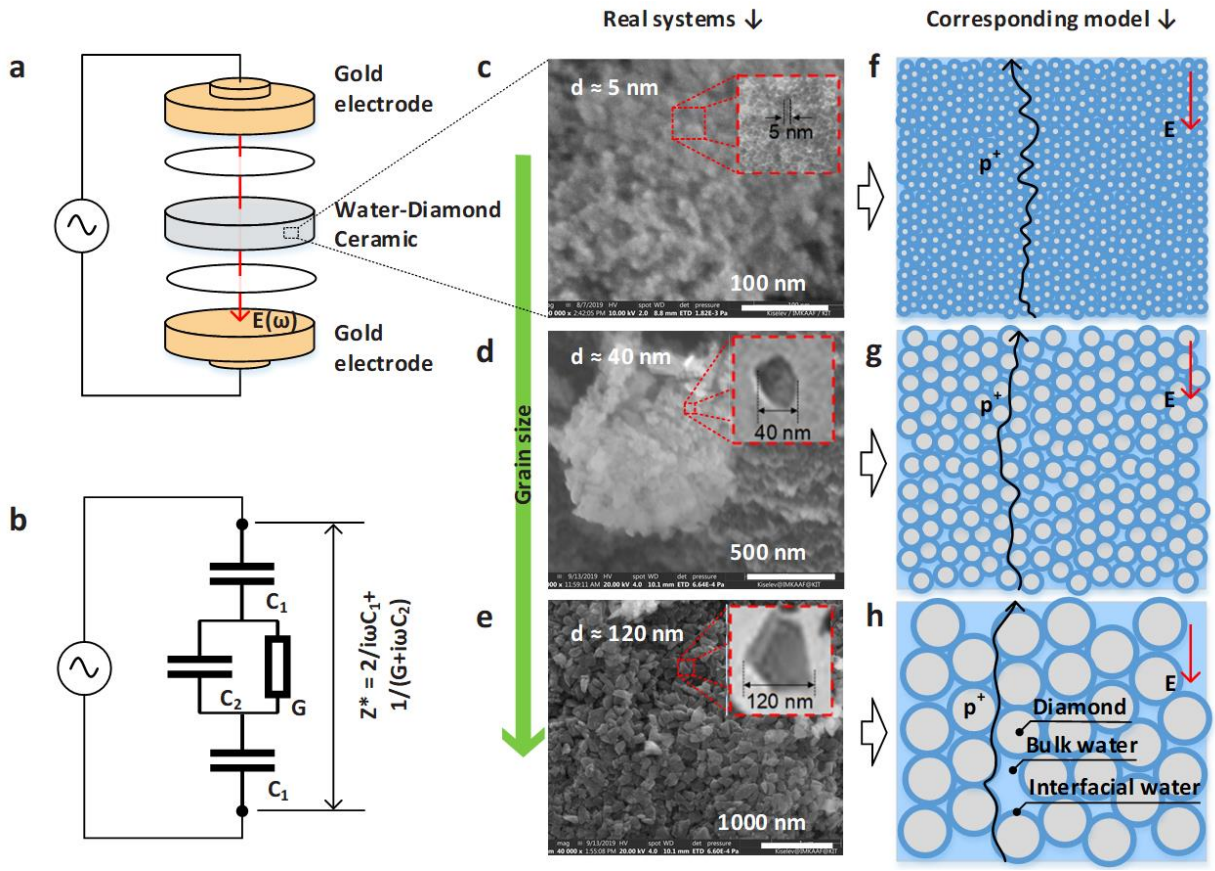

Fig. 1 | Experimental schematic and samples. a, Measuring cell layout. **b**, Equivalent circuit for the media between the electrodes and the equation used to derive the conductivity from the measurements of complex impedance Z*. **c** to **e**, Electron-microscopy images of diamond pellets with different grain sizes with insets showing single grain size $d \approx 5$ nm, $d \approx 40$ nm, and $d \approx 120$ nm, respectively (grain images for different grain sizes are given in Supplementary Information). **f**, to **h**, Corresponding model structures. As the grains become smaller, the relative volume of the interfacial water (deep blue) decreases from about 95% for 5 nm grains to 20% for 120 nm grains, while the relative volume of bulk water (light blue) and diamond grain matrix increases. Black arrows show trajectories of protons (p^+) through the percolated high conductive interfacial water layer. Red arrows indicate the instant directions of the electric field. The effective cross section of the interfacial water

is higher for the small grains and reaches 35% of the sample perpendicular-to-the-electric-field area in case of randomly oriented spherical particles[26].

Results

Figure 2a shows the DC ionic conductivity σ of the water-diamond composite material (pellets) as a function of diamond grains size d. Each point on the graph results from an average of at least ten measurements. The values of σ are obtained from the conductivity spectra $\sigma(\omega)$ using standard analysis[27,28] from the non-dispersion region unaffected by the electrode polarization and high-frequency polarization processes (see SI, Fig.s9). Although a dry diamond pellet is an insulator with negligible intrinsic and surface conductivities, the specimen exhibits high ionic conductivity as it is filled with water (see Fig. 2a): σ monotonically increases proportionally to the inverse pore radius $1/r$ as the pore size decreases. The highest conductivity of 7×10^{-4} S/cm was measured for grain size of 40 nm. A simple model describing conductivity as a function of pore size predicts the maximum value of $\sigma_{max} \approx 0.001$ S/cm when the pore radius r reaches few nanometers (dash-dot line in the Fig. 2a, see discussion for details). This predicted maximum conductivity would be up to five orders of magnitude higher than in bulk water[29]. A further decrease of the pore size leads to a reduction of the ionic conductivity. For pores with radius approaching two nanometers, the conductivity is almost an order of magnitude smaller than $\sigma_{\max}$. We associate this latter effect with the partial breakdown of percolation network when the channels between pores reach the size of several molecular diameters.

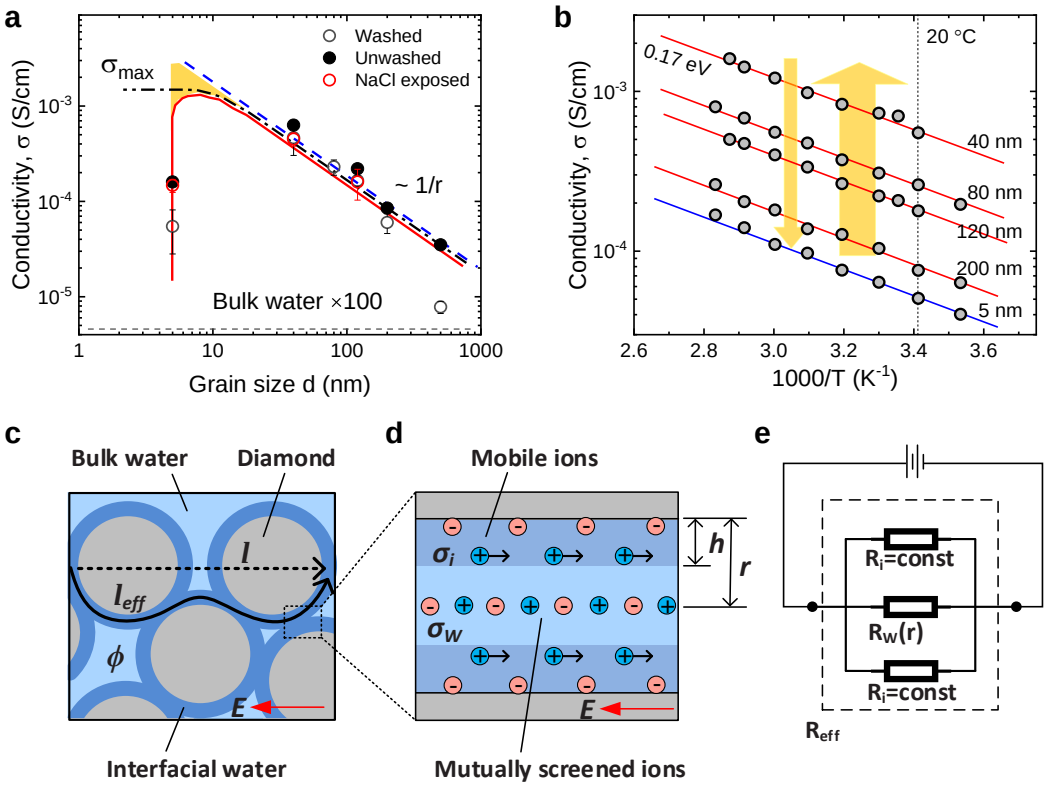

Fig. 2 | Electrodynamics of confined and interfacial water. a, DC conductivity, σ, of porous diamond samples filled with water as a function of grain size *d*. The modeled conductivity behavior is shown by continuous lines. **b**, DC conductivity σ as a function of temperature *T* for five different grain sizes *d* (identical slope of the fit lines corresponds to the equal activation energy of 0.17 ± 0.01 eV). **c**, Conceptual model of the water-diamond system. The grey circles represent diamond grains, deep and light blue regions are interfacial and bulk-like water, respectively. Black arrows illustrate the difference between the sample thickness *l* (dashed line) and the effective path l_{eff} (solid line) for the high proton conductivity. **d**, Model of enhanced conductivity of interfacial water σ_i in comparison with the bulk water σ_w. In the bulk water (light blue region), the ions of H_3O^+ and OH^- (excess protons p^+ and proton holes p°) are screened by each other due to the Coulomb interaction, but in the interfacial layer (dark blue) they can move freely as a result of polarization due to dynamic

equilibrium between the high-mobility p^+ and low-mobility p°[30]. The estimated thickness *h* of the interfacial layer is 1 nm[31]. **e**, The equivalent circuit for the model is presented in Fig.2d where the effective resistivity R_{eff} of the pore is the pore-radius-dependent resistivity of bulk-like water $R_w(r)$ and the constant resistivity of interfacial water R_i connected in parallel.

To clarify the possible contribution of the surface COOH and COO- groups into the conductivity of interfacial water, we measured their concentration by means of infrared spectroscopy and titration. For the samples with smallest grain size, the number of COOH and COO- groups was found to be less than 2 groups per single nano-diamond grain (see SI for details). We performed several tests to separate their contribution to the ionic conductivity of confined water from those of the changed intermolecular interactions in the interfacial water. The surface specific concentration of the carboxyl groups was found to increase with decreasing grain size, but the variability of intensities for different grain sizes is an order of magnitude smaller than variability of the conductivity value (see SI, Fig.s8). We compared pellets prepared from unwashed diamond powders (black dots in Fig. 2a) with those that were cleaned multiple times in the double-distilled water (open circles), and observed only 10% difference. Additionally, the diamond powders were exposed to NaCl solution to replace the protons that could be present on the diamond surface by the less mobile Na^+ ions. This treatment showed negligible effect on water conductivity (red circles in Fig. 2a). The charged surface functional groups thus appear not to be the main source of charge carriers in the interfacial water.

Figure 2b shows the temperature dependence of the ionic conductivity. From the slope of the fit lines, the activation energy (the energy required for a charge carrier to contribute in DC conductivity) was calculated to be equal to (0.17 ± 0.01) eV independent of the grain size. This value is equal to the energy of proton transfer reactions[32], and activation energy of high frequency terahertz conductivity

of bulk water[33], but differs from the activation energy 0.37 eV of DC conductivity of bulk water[29]. These observations strongly suggest that the conductivity of interfacial water is dominated by the proton transport, which is reduced by the boundary interaction with surrounding.

Discussion

Although water is a globally electroneutral-homogeneous system, it exhibits changed physical and chemical properties near the interface depending on the degree of nano-confinement (i.e. size of domain) or physico-chemical properties of the surface[34,35,36]. Interfacial water properties are determined by the changed intermolecular interactions of water itself, by the surface reactivity (concentration of surface sites, surface charges redistribution, etc.), or by combination of these factors. Results described above show that the contribution of surface groups cannot explain more than one tenth of the overall 10^5 enhancement of ionic conductivity (see SI for details). Thus, one should consider the effect of dimension on the water properties.

The surface effects on water properties are local and do not interfere with the properties of bulk water. The effective thickness h of the interfacial water layer is limited by a few nanometers[12,36]. Therefore, the enhanced conductivity of confined water observed in our experiment can be explained by the cumulative effect of the interfacial water with high ionic conductivity σ_i, and the water with bulk conductivity σ_w[37]. This concept is illustrated in Fig. 2d, schematically showing a cylinder pore between two diamond surfaces. The overall resistivity $R_{eff} = l_{eff}/\sigma_{eff} \times A = 1/(R_w^{-1}+2R_i^{-1})$ of such water-filled channel can be described by an equivalent circuit of three resistors in parallel (Fig. 2e). We suggest that ions in the interfacial water layer have higher mobility than in the bulk region, and thus ensure a higher conductivity when the external electric field is applied (see Fig. 2d, and section H in SI).

In this model, the effective conductivity σ_{eff} of the pore is given by the formula $\sigma_{eff}(r) = [2\sigma_i hr+\sigma_w(r-h)^2]/(hr+(r-h)^2)$, where σ_i and σ_w are conductivities of interfacial and bulk water, respectively. The thickness h of the interfacial water layer is assumed to be constant and independent of the pore size. For the smallest pores of about few nanometers the pore size becomes less than $2h$, thus resulting in breakdown of percolation and reduction of conductivity. The dash-dotted curve in Fig. 2a corresponds to the function $\sigma_{eff}(r)\phi/\tau^2$, where, $\tau = l_{eff}/l$ is tortuosity, ϕ is sample porosity (SI, Table S1), and l and $l_{eff} \sim \pi l$ are the thickness of the sample along electric field and the effective capillary length, respectively (see Fig. 2d). In the limiting case of $r = h$, all water in the pores is confined within the interfacial layer; in this case the conductivity of the effective media is equal to $\sigma_{eff}(h)=\sigma_{max}$, and the parameter σ_i can be simply found as $\sigma_i = \sigma_{max}(l_{eff}/l)^2/2\phi = \sigma_{max}\tau^2/2\phi \approx \sigma_{max}\pi^2/2\phi$. For randomly packed, slightly irregular particles $\phi \approx 0.35$[38,39]. The expected conductivity σ_i of interfacial water thus becomes equal to 0.02 S/cm, five orders of magnitude larger than that of bulk water.

Figure 2a demonstrates that this simple model describes the experimental data well, allowing to estimate the thickness h of interfacial water with the enhanced conductivity. Within the experimental uncertainty, our data (dash-dot curve) gives $h \approx 1 \pm 0.25$ nm, which is in agreement with experiment and molecular dynamics simulations on the surface structure of water[3,40]. In other words, the conductive interfacial water layer extends for several molecular layers away from the surface. This result is also consistent with the thickness $h_{max} = 2h$ = 2-3 nm where the maximum value of the effective material conductivity approaches σ_{max} (see Fig. 2a). This h_{max} can be understood as the distance where top and bottom near-surface layers overlap. If the pore size is less than h_{max} – as for 5 nm diamond grains – the effective cross section of the interfacial water layer is decreased leading to a reduction of conductivity of the composite porous media (see Fig. 2a).

As water exhibits a distinct layered structure near all surfaces independently of their nature[40], it is reasonable to expect that interfacial water has an enhanced protonic conductivity not only near the diamond surface (such as those studied in this work) but in most cases. We suggest that in interfacial water, the unscreened ions are responsible for the higher direct current as compared to screened ions in bulk water[41]. The mechanism is similar to the one observed for the ionic liquids[42,43] and superionic conductors[44].

The conductivity of interfacial water σ_i exceeds the ionic conductivity of different superionic conductors in the temperatures range between 0 and 100 °C, as shown in Fig. 3. Although water has a low bulk conductivity (red and blue lines in Fig. 3), water becomes a superionic conductor if confined in nano-sized pores. All known values of ionic conductivity of confined water in any material (including Nafion®) fall inside the yellow-shaded region with the upper limit (dashed red) being $\sigma_i(T)$. Our model predicts that water-filled porous materials has a protonic conductivity within this range with the activation energy of about 0.17 eV[45]. The highest possible value for pure interfacial water in narrow nanopores is σ_i. The $\sigma_i(T)$ line is only an order of magnitude lower than the microwave conductivity of water σ_{mw} = 0.1 S/cm at 300 K, previously assigned to the local dynamics of the intrinsic water ions[41].

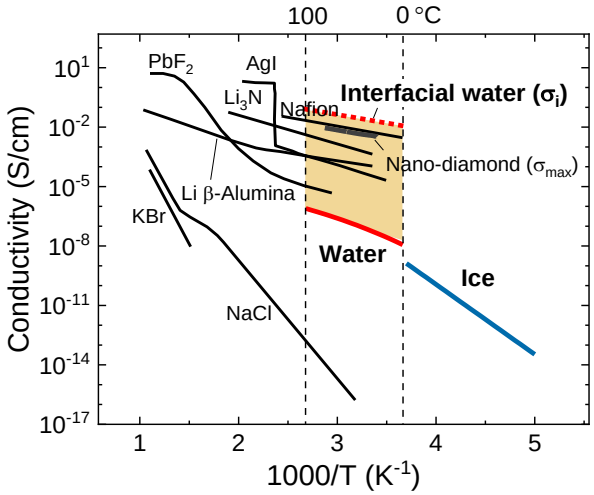

Fig. 3 | Electric conductivity of ionic conductors as a function of inverse temperature. Red and blue lines denote experimental curves for bulk water and ice, respectively. The values inside the yellow-shaded region were obtained for various water-filled samples[5]. The dashed red curve is the upper limit of confined water conductivity and corresponds to pure interfacial water, expected for the materials with narrow pores about 2 nm and high porosity.

Conclusions

We have studied the DC ionic conductivity of interfacial water and found it to be anomalously high. We show that water in nano-confinement exhibit properties of two types: that of bulk water and interfacial water, which differ in their protonic conductivity. Near the interface, the protons have higher mobility and are responsible for the enhanced conductivity in the external electric field. The intrinsic protonic conductivity of interfacial water, σ_i = 0.02 S/cm, is five orders of magnitude larger than what is observed for bulk water. Our results provide a new insight into the fundamental properties of water and help to better understand the general electrodynamic effects in porous membranes and other water-based systems in geological, biological and engineered environments. In

particular, we demonstrate that the conductivity can be enhanced by maximizing the fractional amount of interfacial water and optimization of pore size to avoid the percolation breakdown. Outstanding properties of water at nanoscale pave the way to the development of innovative electrochemical systems, such as proton-exchange membrane fuel cells and redox-flow batteries, which performance is crucially dependent on the high ionic conductivity of membrane material.

Acknowledgments: Authors thank Prof. J. Maier for stimulating discussions and V.G.A. thanks him for partial support of this research, G. Untereiner for help with samples management and preparation, R. Merkle for help with infrared measurements and useful advices. The work was partially supported by the Deutsche Forschungsgemeinschaft (DFG) via DR228/61-1. E.U. acknowledges the support by the European Social Fund and by the Ministry of Science and Research and the Arts Baden-Württemberg. V.G.A. and H.O. acknowledge partial support by the Skoltech NGP program (Skoltech-MIT project). A.K. acknowledges support by the Helmholtz Association under Atmosphere and Climate Programme (ATMO).

Author contributions: V.G.A conceived the idea of the experiment and suggested conceptual interpretation of the results. V.G.A., E.U., and P.K. built the experimental setup, conducted the experiments, and analyzed the data with contributions from A.K., H.O., M.D., and K.S. A.K. characterized the samples with gas adsorption and SEM. M.D., K.S., and H.O. supervised the experimental study and helped to write the manuscript. All authors discussed the results and contributed to the final version of the manuscript. Authors declare no competing interests. All experimental data is available in the main text or the supplementary information.

Competing interests

The authors declare no competing interests.

Additional information

Supplementary materials and methods, Supplementary Figs. s1–s12, Supplementary Table s1, Supplementary refs. 46–54.

References:

1. C. Li, J. Le, Y. Wang, et al. In situ probing electrified interfacial water structures at atomically flat surfaces. *Nature Mater.* **18**, 697–701 (2019).

2. Z. Zhang, L. Piatkowski, H. Bakker, et al. Ultrafast vibrational energy transfer at the water/air interface revealed by two-dimensional surface vibrational spectroscopy. *Nature Chem* **3**, 888–893 (2011).

3. L. Fumagalli, A. Esfandiar, R. Fabregas, S. Hu, P. Ares, A. Janardanan, Q. Yang, B. Radha, T. Taniguchi, K. Watanabe, G. Gomila, K. S. Novoselov, A. K. Geim, Anomalously low dielectric constant of confined water. *Science* **360**, 1339-1342 (2018).

4. S. Cerveny, F. Mallamace, J. Swenson, M. Vogel, and L. Xu, Confined Water as Model of Supercooled Water. *Chem. Rev.* **116**, 7608−7625 (2016).

5. H. Chinen, K. Mawatari, Y. Pihosh, K. Morikawa, Y. Kazoe, T. Tsukahara, and T. Kitamori, Enhancement of Proton Mobility in Extended-Nanospace Channels. *Angew. Chem. Int. Ed.* **51**, 3573 –3577 (2012).

6. X. Ling, M. Bonn, K.F. Domke, and S.H. Parekh, Correlated interfacial water transport and proton conductivity in perfluorosulfonic acid membranes. *PNAS*. **116**, 8715-8720 (2019).

7. H. Ouerdane, B. Gervais, H. Zhou, M. Beuve, J.-Ph. Renault, Radiolysis of Water Confined in Porous Silica: A Simulation Study of the Physicochemical Yields. *J. Phys. Chem. C.* **114**, 12667-12674 (2010).

8. H. Volland, *Atmospheric Electrodynamics* (Springer, Berlin, 1984).

9. J. A. Anderson, E. Rosenfeld, *Neurocomputing: Foundations of Research* (The MIT Press, Cambridge, Massachusetts, 1988).

10. V. R. Stamenkovic, D. Strmcnik, P. P. Lopes & N. M. Markovic, Energy and fuels from electrochemical interfaces, *Nature Materials.* **16**, 57–69 (2017).

11. I. Brovchenko and A. Oleinikova, *Interfacial and Confined Water* (Elsevier, Amsterdam, 2008).

12. F. Kremer, Ed., Dynamics in Geometrical Confinement (Advances in Dielectrics vol VIII) (Springer, Berlin, 2014).

13. P. Atkins and J. de Paula, *Physical Chemistry* (Oxford University Press, Oxford, 8th edition, 2006).

14. W. E. Kenyon, Texture effects on megahertz dielectric properties of calcite rock samples. J. Appl. Phys. **55**, 3153-3159 (1984).

15. I. Holwech and B. Nost, Dielectric dispersion measurements of salt-water-saturated porous glass. *Phys. Rev. B.* **39**, 12845-12852 (1989).

16. M. Loewer, T. Gunther, J. Igel, S. Kruschwitz, T. Martin and N. Wagner, Ultra-broad-band electrical spectroscopy of soils and sediments - a combined permittivity and conductivity model. *Geophys. J. Int.* **210**, 1360–1373 (2017).

17. K. Wu, Zh. Chen, J. Li, X. Li, J. Xu, and X. Dong, Wettability effect on nanoconfined water flow. *PNAS* **114**, 3358-3363 (2017).

18. G. Cicero, J. C. Grossman, E. Schwegler, F. Gygi, and G. Galli, Water Confined in Nanotubes and between Graphene Sheets: A First Principle Study. *J. Am. Chem. Soc.* **130**, 1871-1878 (2008).

19. S. Raz, K. Sasaki, J. Maier, I. Riess, Characterization of adsorbed water layers on Y_2O_3-doped ZrO_2. *Solid State Ionics* **143**, 181-204 (2001).

20. G. Gregori, M. Shirpour, and J. Maier, Proton Conduction in Dense and Porous Nanocrystalline Ceria Thin Films. *Adv. Funct. Mater.* **23**, 5861 (2013).

21. A. Revil, Effective conductivity and permittivity of unsaturated porous materials in the frequency range 1 mHz–1GHz. *Water resources research*. **49**, 306–327 (2013).

22. O. Björneholm, M. H. Hansen, A. Hodgson, L.-M. Liu, D. T. Limmer, A. Michaelides, P. Pedevilla, J. Rossmeisl, H. Shen, G. Tocci, E. Tyrode, M.-M. Walz, J. Werner and H. Bluhm, Water at interfaces. *Chemical Reviews*. **116**, 7698-7726 (2016).

23. V. M. Gun'ko, V. V. Turov, V. M. Bogatyrev, V. I. Zarko, R. Leboda, E. V. Goncharuk, A. A. Novza, A. V. Turov and A. A. Chuiko, Unusual properties of water at hydrophilic/hydrophobic interfaces. *Advances in Colloid and Interface Science*. **118**, 125-172 (2005).

24. O. A. Shenderova and G. E. McGuire, Science and engineering of nanodiamond particle surfaces for biological applications. *Biointerphases.* **10**, 030802 (2015).

25. F. Kremer & A. Schonhals, Eds., *Broadband Dielectric Spectroscopy* (Springer Verlag, Berlin, 2003).

26. D. J. Priour, Jr. and N. J. McGuigan, Percolation through Voids around Randomly Oriented Polyhedra and Axially Symmetric Grains. *Phys. Rev. Lett.* **121**, 225701 (2018).

27. M. Samet, V. Levchenko, G. Boiteux, G. Seytre, A. Kallel, and A. Serghei, Electrode polarization vs. Maxwell-Wagner-Sillars interfacial polarization in dielectric spectra of materials: Characteristic frequencies and scaling laws. *J. Chem. Phys.* **142**, 194703 (2015).

28. P. Lunkenheimer, A. Loidl, Dielectric spectroscopy of glass-forming materials: α-relaxation and excess wing. *Chemical Physics* **284**, 205-219 (2002).

29. T. S. Light, S. Licht, A. C. Bevilacqua, and K. R. Morash, The Fundamental Conductivity and Resistivity of Water, *Electrochemical and Solid-State Letters*. **8,** E16-E19 (2005).

30. S. H. Lee, J. C. Rasaiah, Proton transfer and the mobilities of the H+ and OH- ions from studies of a dissociating model for water. *J. Chem. Phys.* **135**, 124505 (2011).

31. J. G. Constantin, M. M. Gianetti, M. P. Longinotti and H. R. Corti, The quasi-liquid layer of ice revisited: the role of temperature gradients and tip chemistry in AFM studies. *Atmos. Chem. Phys.* **18**, 14965-14978 (2018).

32. Z. Luz, and S. Meiboom, The Activation Energies of Proton Transfer Reactions in Water. *J. Am. Chem. Soc.* **86**, 4768–4769 (1964).

33. V. G. Artemov, A. A. Vokov, Water and Ice Dielectric Spectra Scaling at 0 °C, *Ferroelectrics*. **466**, 158-165 (2014).

34. V. Buch, A. Milet, R. Vacha, P. Jungwirth, J. P. Devlin, Water surface is acidic. *PNAS* **104**, 7342–7347 (2007).

35. M. Vossen, F. Forstmann, A. Kramer, Structure of water and electrolyte near an electrode. *Solid State Ionics* **94**, 1-7 (1997).

36. A. W. Knight, N. G. Kalugin, E. Coker & A. G. Ilgen, Water properties under nano-scale confinement, *Sci. Rep.* **9**, 8246 (2019).

37. V.G. Artemov, A.A. Volkov, A.V. Pronin, Electrical properties of water: a new insight. *Biophysics* **59**, 520-523 (2014).

38. P. W. J. Glover and E. Walker, Grain-size to effective pore-size transformation derived from electrokinetic theory. *Geophysics.* **74**, E17–E29 (2009).

39. S. B. Jones and S. P. Friedman, Particle shape effects on the effective permittivity of anisotropic or isotropic media consisting of aligned or randomly oriented ellipsoidal particles. *Water resources research.* **36**, 2821-2833 (2000).

40. O. Björneholm, M. H. Hansen, A. Hodgson, L.-M. Liu, D. T. Limmer, A. Michaelides, P. Pedevilla, J. Rossmeisl, H. Shen, G. Tocci, E. Tyrode, M.-M. Walz, J. Werner, and H. Bluhm, Water at Interfaces, *Chem. Rev.* **116**, 7698-7726 (2016).

41. V. G. Artemov, A unified mechanism for ice and water electrical conductivity from direct current to terahertz, *Phys. Chem. Chem. Phys.* **21**, 8067-8072 (2019).

42. G. Ori, C. Massobrio, A. Pradel, M. Ribes, and B. Coasne, Structure and Dynamics of Ionic Liquids Confined in Amorphous Porous Chalcogenides. *Langmuir*, **31**, 6742–6751 (2015).

43. Q. Berrod, F. Ferdeghini, P. Judeinstein, N. Genevaz, R. Ramos, A. Fournier, J. Dijon, J. Ollivier, S. Rols, D. Yu, R. A. Mole and J.-M. Zanotti, Enhanced ionic liquid mobility induced by confinement in 1D CNT membranes. ***Nanoscale,* 8**, 7845-7848 (2016).

44. M. B. Salomon, *Physics of Superionic Conductors* (Springer-Verlag, Berlin, 1979).

45. V. G. Artemov, Dynamical conductivity of confined water. *Meas. Sci. Technol.* **28**, 014013 (2017).

Supplementary Materials for

Anomalously High Proton Conduction of Interfacial Water

V.G. Artemov[1]*, E. Uykur[2], P.O. Kapralov[3], A. Kiselev[4], K. Stevenson[1], H. Ouerdane[1], M. Dressel[2]

[1] Center for Energy Science and Technology, Skolkovo Institute of Science and Technology, 121205 Moscow, Russia

[2] 1. Physikalisches Institut, Universität Stuttgart, 70569 Stuttgart, Germany

[3] Russian Quantum Center, 143025 Moscow, Russia

[4] Institute of Meteorology and Climate Research, Karlsruhe Institute of Technology, 76021 Karlsruhe, Germany

* Correspondence to: v.artemov@skoltech.ru

Table of Contents

Materials and Methods

Samples preparation

For the formation of pellets (Fig. s1) we used powders with different, but narrow grain-size distributions (Figs. s2 and s3) all purchased from the same manufacturer (Adámas Nanotechnologies, 8100 Brownleigh Drive Raleigh, NC 27617). Pellets were 1 mm thick, 5 mm in diameter, and pressed from the powders at about 30 tons per cm^2. To increase the sample mechanical stability, we additionally added 5 mass percent of polytetrafluoroethylene. Diamond grains had high crystallinity as clearly seen on the diffraction pattern (see Fig. s3). The grain-size dispersion, obtained by the open ImageJ software for grain size analysis from scanning electron microscopy patterns, did not exceed 0.5. We made about 100 pellets of six different grain sizes from 5 to 500 nm, and used different pellets of the same kind to test the reproducibility of results.

Samples cleaning and characterization

The powder obtained from the manufacturer was preliminary cleaned to minimize a possible effect of the surface contaminants on the conductivity of confined water. First, we boiled diamond powders in hydrochloric acid solution. Second, we centrifugally cleaned diamonds dissolved in double-distilled water many times until complete stabilization of pH in the rest of water after precipitation of the powder. The initial pH value was between 4 and 5, at the end it was between 6 and 7, slightly different for samples with different grain sizes. Finally, we dried the washed nano-diamond powder in the oven for four hours at 350 °C. Samples chemical composition was tested by energy-dispersive X-ray analysis (see Fig. s4). No traces of foreign species were found except

oxygen (O) and a negligible amount of metals (Ni, Al) that are presumably tracers of the materials which were used at the manufacturing stage. The large amounts of silicon (Si) and platinum (Pt) shown in Fig. s4 are due to the silicon substrate, as well as the metal coating, which were used. See also section I for details of the titration experiment.

Samples porosity and surface area

The pore size distribution in the compressed pellets were measured by gas adsorption with the Quantachrome® AUTOSORB-iQ-MP-XR instrument (see Figs. s5, s6 and Table s1), using argon at 87 K, nitrogen at 77 K, and water vapor at 288 K as absorbate. Figure s5 shows adsorption/desorption isotherms of gases on nano-diamond pellets. All pellets had similar open porosity and wide network of percolated nano-pores, as found by applying Density Functional Theory (DFT) and Brunauer-Emmett-Teller (BET) analysis implemented into the standard Quantachrome® ASiQWin software. Both methods gave consistent results for the specific surface area, pore volume, and effective pore radius for all pellets with different grain sizes. The specific pore volume was calculated as: $V_0 = (V_{pellet}\text{-}m_{dry}/\rho_d)/m_{dry}$ from the pellet mass and geometry, and coincides with gas sorption estimates. The porosity ϕ of the samples was found from the gravimetric analysis. The modal micropore radius r_{eff} was obtained from Argon adsorption at 87 K. The transformation factor $\Theta = d_{eff}/2r_{eff}$ from grain size d_{eff} to pore radius r_{eff} was taken equal to the transformation factor Θ for the randomly oriented angular particles[46], which are close to the observed ones (see Fig. s2).

The specific surface area is plotted as a function of the grain size in Fig. s7a and shows inverse proportionality to the grain size, the same scaling law observed for the conductivity of confined water (see Fig. 7b). Figure s7c shows direct proportionality of the electrical conductivity and the

specific surface area of the porous nano-diamond matrix. The higher is the surface, the higher is the conductivity of confined water.

Filling nanopores with water

To fill the pores with water we first pumped pellets to remove the air from pores, and then stored them to the saturated pure-water-vapor atmosphere for 48 hours. We found that the weight gain $\Delta m=(m_{wet}-m_{dry})$ of the pellet reaches its maximum already after 5 hours of storage in desiccator, but waited longer to let the water molecules diffuse to the nanopores[47]. We calculated the specific volume occupied by water $V_w= \Delta m /\rho_w/ m_{dry}$, where ρ is water density, and found that V_m is approximately equal to pore volume V_0. Thus, the pores of our samples were completely full with water. Note that the purity of water inside the pores is not discussed here because the adsorption from the vapor phase eliminate additional impurities from outside the sample.

Insofar as the porous samples could lose water during the measurements, we isolated pellets from the air with a closed Teflon cell. To avoid water evaporation, the Teflon cell and the sealing ring were tightly closed during the measurements. The stability test showed that the reduction of weight after the sample heating to 90 °C and then cooling down to the room temperature, was less than 5%.

Electrical conductivity of confined water and density of the diamond surface groups

It is well known[48] that nano-diamonds have surface carboxylic groups that could affect the electrical conductivity of confined water. While the high density of the surface groups is crucial for the medical applications, it is undesirable in our study. We measured the infrared intensities of

surface COOH and COO- groups (see Fig. s8) and found this concentration too low to explain the enhanced electrical conductivity of confined water. Moreover, the intensity of the surface groups normalized to the unit area (Fig. s8b) decreases with decrease of the grain size, while the conductivity increases (see Fig. s7b). Thus, here the surface groups are not the main contributors to the conductivity of the confined water.

Measurements of the dielectric constant and conductivity

For the measurement of the complex impedance of the sample, we used Novocontrol alpha-A analyzer with frequency range 0.1 Hz – 3 MHz. The parallel-plate-capacitor geometry with circular polished electrodes covered with 50 nm of chromium and 10 nm of gold were used as shown in Fig. s9. The temperature of the sample was controlled in the range from 283 to 363 K with the accuracy of 1°. The effective dielectric constant ε_d^{eff} of the dry pellets was used as a reference. The low ε_d^{eff} =3.85 (Fig. s10, d to f) is a result of the diamond ($\varepsilon_d \approx 5.7$) and air ($\varepsilon \approx 1$) dielectric constants averaging, and corresponds to the porosity ϕ of the samples according to the formula $\varepsilon_d^{eff}=(1-\phi)\varepsilon_d+\phi\varepsilon_0$. The electric conductivity of the dry pellets was negligibly small in comparison with conductivity of bulk water and corresponding wet pellets (see Fig. s10, g to i).

Dielectric data analysis

The dielectric spectra shown in Fig. s10 have regions affected by electrode polarization. The dielectric constant spectrum shows dispersion at low frequency limits due to formation of the near-electrode layer and the DC conductivity contribution[49]. To find the dielectric constant unaffected by electrodes, the blocking electrodes schematic was used: we applied Mylar films between the

gold plates and pellets (see Fig. s9d). The corresponding equivalent circuit for this case have the total impedance $Z = 1/(i\omega C_1) + 1/(G+i\omega C_2)$ and admittance $1/Z = G_p + i\omega C_p$, where $\omega=2\pi\nu$ is angular frequency. In the high frequency limit $\omega\rightarrow\infty$ and for $C_1>>C_2$ we have $C_p=C_2$ and $G_p = G$. In other words, the high-frequency dielectric constant corresponds to the dielectric constant of the sample. Thus, we can consider the high-frequency plateau of the dielectric spectrum obtained with blocking electrodes as the value of the dielectric constant unaffected by the electrode effects (see Fig. s10). The conductivity spectrum also shows dispersion at low frequencies due to electrode polarization mechanisms and Maxwell-Wagner effects[50]. It was shown that at high frequency the conductivity spectrum tends to the true value of DC conductivity. The dashed horizontal line in Fig. s7c shows the extrapolation of the DC conductivity plateau to low frequencies. Another way to obtain the DC conductivity is to plot the Nyquist plots shown in Fig. s12.

Interfacial water layer thickness

The cornerstone of this paper is the notion of interfacial water whose structure and properties are not established yet. The main idea of our experiment is to investigate the size effect on water conductivity and study the interfacial water in such a way. The increase of electric conductivity of confined water with the decrease of pore size can be explained, as shown in the main text, by the presence of the thin interfacial water layer (deep blue) and the bulk water layer (light blue) (see Fig. 2). The latter almost disappears for the case of pores comparable with the interfacial water thickness. Different models show interfacial water thickness h_i from 7 to 8 Å[51]. This value agrees well with the diffusion distance of short-living excess protons and proton holes in the recently proposed ionic model of water[52]. Molecular dynamics simulations using semiclassical methods independently confirmed high concentration of short-living excess charges in liquid water with

concentration of about 1 M[53]. The average distance between ions at such concentration is l = 7.5 Å, which is equal to the commonly accepted interfacial water layer thickness h_i. According to the model, the electrical charges in bulk water are screened by each other as can be seeing from the calculation of the Debye length $\lambda_D=(\varepsilon\varepsilon_0 k_B T/2q^2 n_{\pm})^{1/2} \approx 1$ nm, but can move fast at short distances inside the screening atmosphere. It was shown that this high mobility, and predicted that at nanoscale the conductivity of water will increase[45]. Unscreened ionic species near the interface show higher mobility than the mutually screened ions in the bulk water. This causes the enhanced electric conductivity of water near interfaces.

pH titration of diamond nano-powders in NaCl solution

The surface of nano-diamonds is known to have surface-active groups and foreign impurities (see Ref. [25] of the main text). Groups and impurities can affect the conductivity of the water in which they dissolve by donating mobile ionic species. That is why an important part of our work was the analysis of the possible effect of surface reactions on the properties of water. To evaluate the surface density of the absorption sites on the diamond surface, we performed a pH titration test[54] for 5 and 40 nm diamond nano-particles. The following procedure was applied. First, 0.2 g powder was "dissolved" in 50 ml of 1M NaCl solution to ensure complete deprotonation. Then, by automatic adding of small volumes of 0.01M NaOH solution, we obtained a pH dependence on the amount of NaOH. The solution was stirred magnetically all the time; titration was performed within 30 min after solution preparation. A step-like increase of pH, which corresponds to the transition from the “excess hydronium” to “excess hydroxyl” modes, was found at V_t = 1.230 and 1.026 ml of NaOH for 5 and 40 nm particles, respectively. The specific surface area of 1 g of the 5 nm powder was found as $S_{tot}= \pi d^2/m_0 =350$ m^2/g, where $m_0 = 4/3\ \pi\ (d/2)^3 \cdot \rho$ is the mass of single

grain, d is the grain diameter, and ρ=3.51 g/cm^3 is the diamond density. The calculated S_{tot} is in good agreement with the experimentally obtained effective surface area (see Table s1). A 40 nm powder surface area was found by analogy. Finally, taking into account the total surface area S_{tot} of diamonds and comparing this area with the area of a single sodium ion $S_{Na}=90^{2}\cdot10^{-24}=2.5$ Å^2 multiplied by the amount of sodium that corresponds to the V_t, we found the effective area S_{eff} occupied by the titrant, and, as a result, the surface density of absorption sites $P=S_{eff}/S_{tot}$. The latter is similar for 5 and 40 nm grains and equal to 0.002. In other words, only 1/1000 of the surface sites is occupied. Taking into account that 5 nm grains contain about 1000 carbon atoms, this means that one “free” ion exists per grain. Diamond surface ions thus appears not to be the main charge carriers in the confined water.

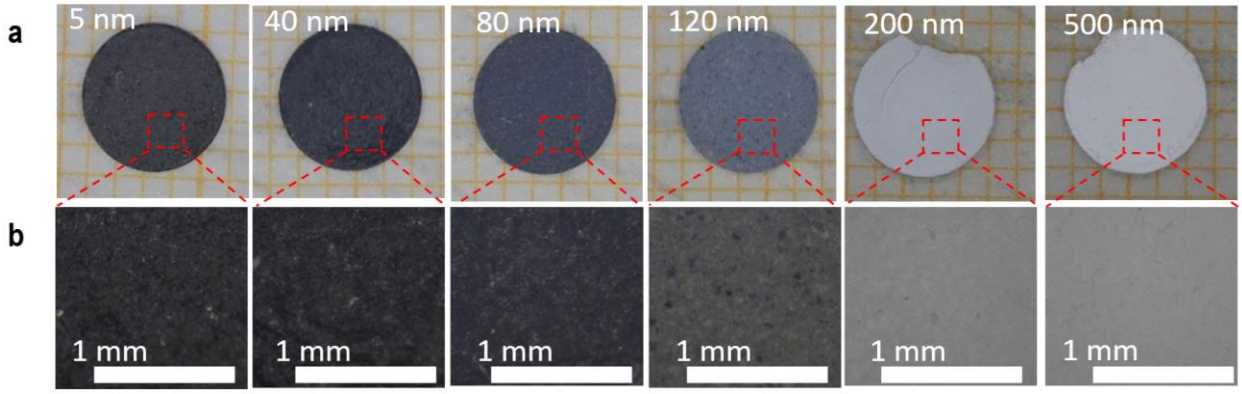

Fig. s1 | Porous nanodiamond (ND) pellets for dielectric study of water at nanoscale. a, Pellets of 1 mm thick and 5 mm diameter formed from the powders of different grain sizes. To obtain the mechanical stability of pellets, 5 mass % of polytetrafluoroethylene (PTFE) was used. **b**, Enlarged optical photos of parts of the pellets. Scale bar is 1 mm everywhere.

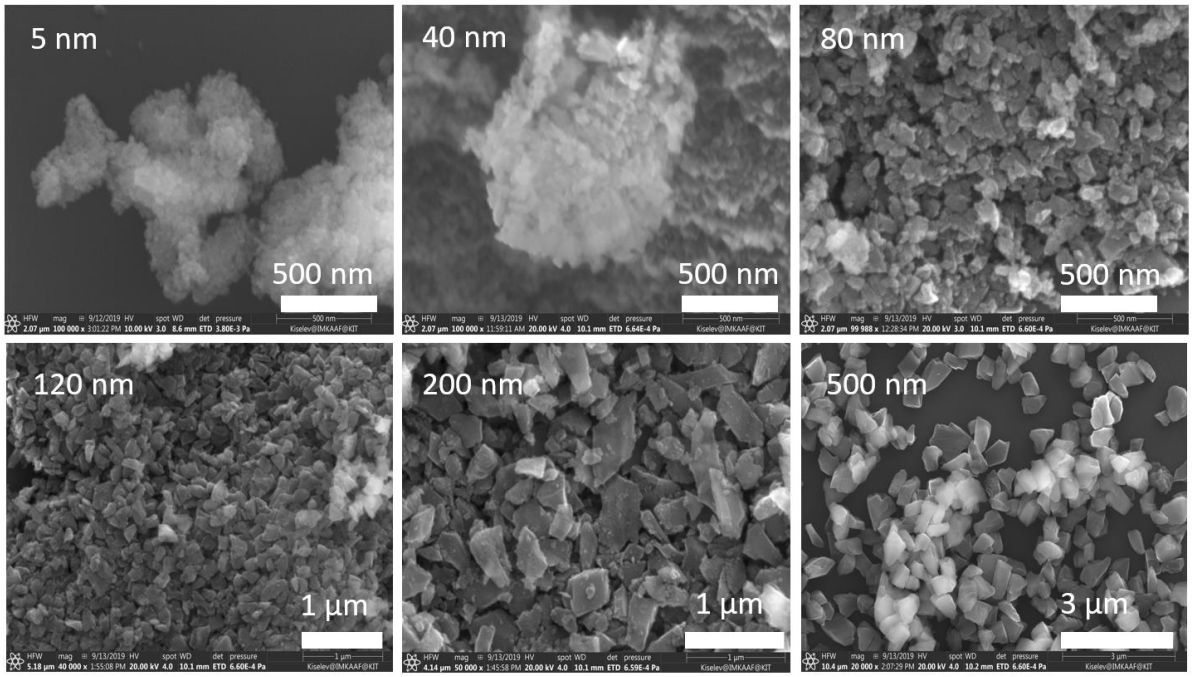

Fig. s2 | Scanning Electron Microscope (SEM) pictures of ND powders. Samples are shown for different average grain sizes. The resolution is indicated by the scale bars.

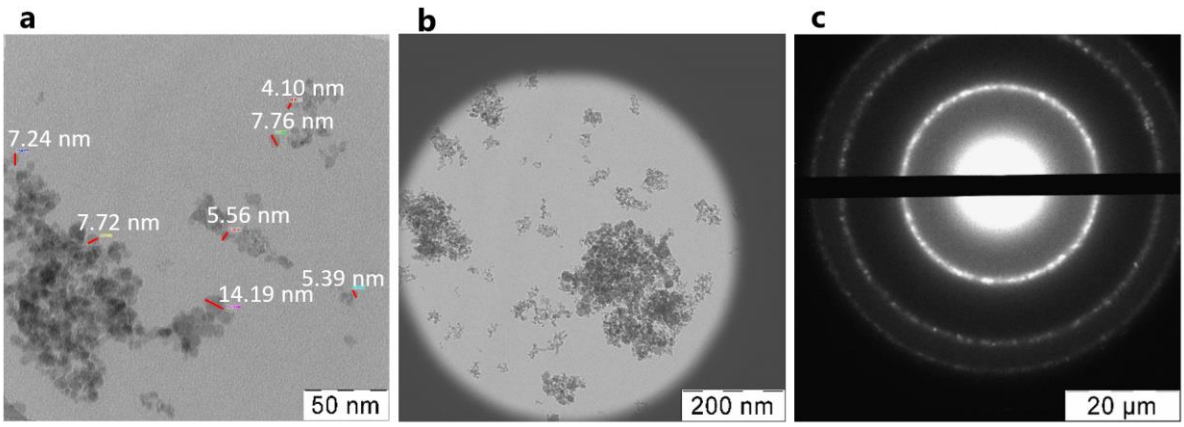

Fig. s3 | Morphology of the diamond powder. a and **b**, Transmission electron microscopy (TEM) pictures of 5 nm diamond powder. Numbers are size of the corresponding single grains. Aggregates of grains from 50 to 300 nm size are observed. **c**, Diffraction pattern of 5 nm diamond powder shows crystallinity of the sample.

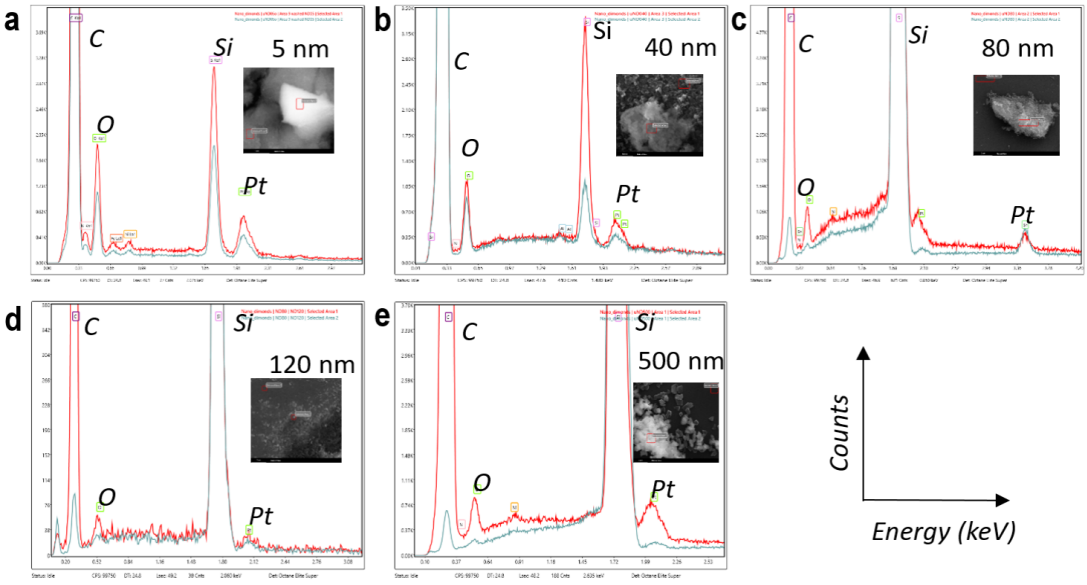

Fig. s4 | Elemental analysis of nano-diamonds. a to **e**, Energy-dispersive X-ray (EDS) intensities of atoms of elements found in samples of nano-diamonds of different grain sizes. Red and blue spectra correspond to different selected areas of the electronic beam interaction with the sample (see insets).

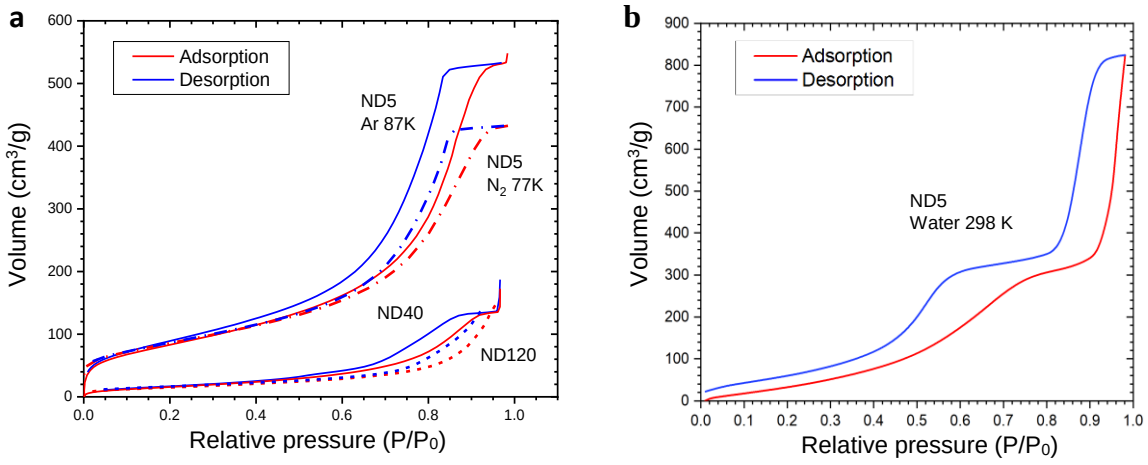

Fig. s5 | Adsorption/desorption isotherms of gases on pellets of ND. a, Argon at 87K (solid and dash lines) and nitrogen at 77 K (dash-dot lines) on 5, 40 and 120 nm grains. **b**, Water vapor at room temperature on 5 nm grains. Samples exhibit mesoporosity as indicated by the adsorption-desorption hysteresis. The difference in adsorption isotherms obtained for different gases is due to the different size and polarizability of Ar, N_2 and H_2O molecules. The strong rise at P/P_0 >0.9 (right-site graph) corresponds to the effect of capillary condensation.

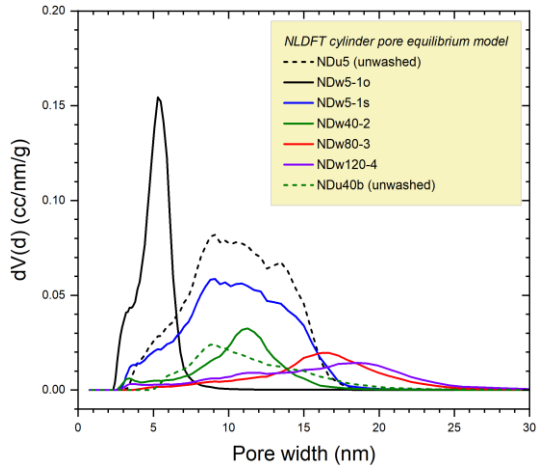

Fig. s6 | Pore size distribution of ND pellets by Ar adsorption at 87 K. Non-Linear equilibrium DFT (NLDFT) model in cylindrical pores. For ND5, For ND40 ND120, only mesopores in the size range from 5 to 20 nm can be retrieved with DFT. For ND120, both DFT and Barrett, Joyner, and Halenda (BJH) method give broad mesopores in the range from 3 to 40 nm. The mesopores in the samples containing larger grains (> 120 nm) could not be retrieved by NLDFT.

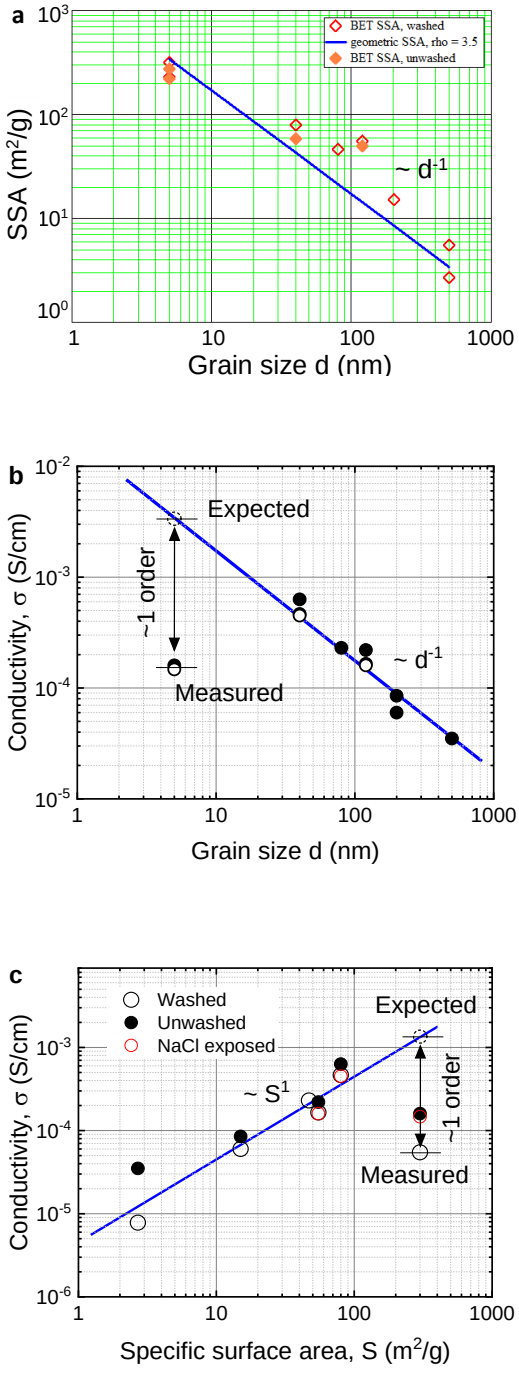

Fig. s7 | Specific surface area (SSA) of nano-diamonds and conductivity of confined water. **a**, SSA in m^2/g for ND pellets vs. grain size d obtained from Ar adsorption isotherms at 87 K. The blue line corresponds to surface-to-volume ratio (1/d) of the grains for the spherical particle

approximation. **b**, Electrical conductivity of wet ND pellets vs. grain size d (data from Fig.2A of the main text). The blue line means the same as above. **c**, Electrical conductivity of wet ND pellets vs. SSA. Direct proportionality is obvious. A one-order of magnitude difference for conductivity is observed for the smallest grain size of 5 nm.

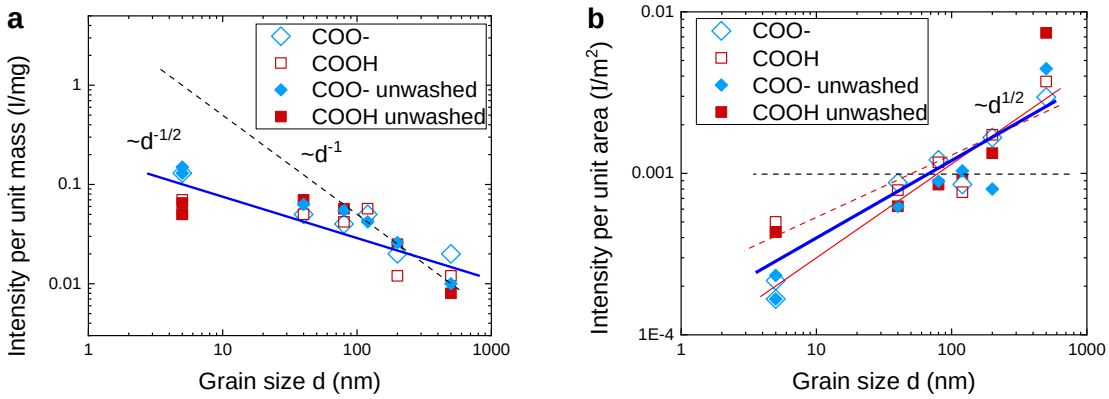

Fig. s8 | Concentration of COOH and COO- groups on the diamond surface. a, Intensity of IR vibrations of COO- and COOH groups normalized to 1 mg of the powder vs. grain size. **b**, The same for intensity normalized to the unit area of ND surface. Spectra measured for the powders pressed in pellets of KBr in transmission mode. Lines are guides for eyes.

Table 1 | Properties of nano-diamond pellets. SSA is specific surface area; SPV=(V_{pellet}-m_{dry}/ρ_d)/m_{dry} is specific pore volume; r_{eff} is effective pore width from QSDFT slit model; ϕ = SPV/V_{pellet} is porosity; ρ_d = 3.5 g/cm^3 is diamond density.

ND grain size, nm	**SSA (spherical grains), m^2/g**	**SSA (BET), m^2/g**	**SSA (DFT), m^2/g**	**SPV (exp), cm^3/g**	**SPV (DFT), cm^3/g**	**r_{eff}, nm**	***ϕ*, %**
5	342	317	265	0.4±0.1	0.337	3.4	60± 10
40	43	79	73	0.2±0.1	0.174	6.9	40 ± 10
80	21	46	45	0.2±0.1	0.161	9.8	40 ± 10
120	14	55	53	0.2±0.1	0.173	10.8	40 ± 10
200	8.6	15	16	0.2±0.1	0.1	NA	40 ± 10
500	3.42	5.5	4.6	0.2±0.1	NA	NA	40 ± 10

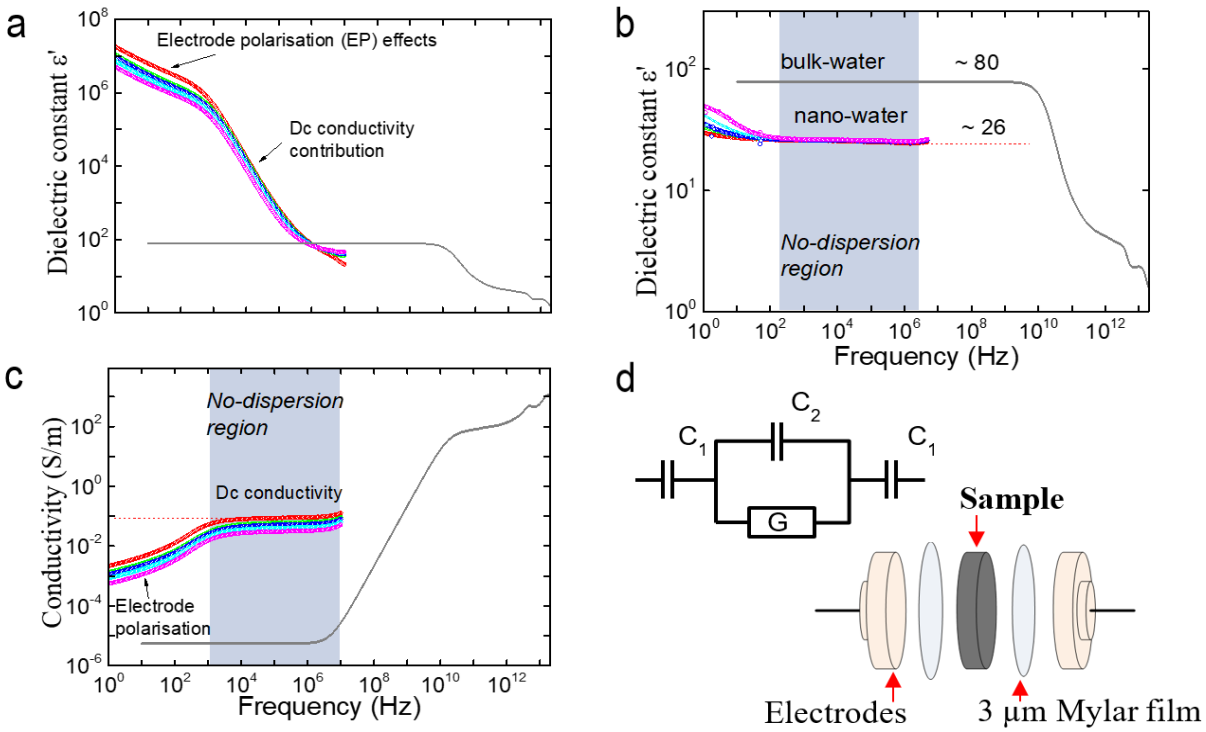

Fig. s9 | Dielectric spectra of the sample for different electrode assemblies. a and **b**, are dielectric functions without and with blocking electrodes (BE), respectively. **c**, Spectrum of dynamic conductivity without BE. **d**, Scheme of measurements with Mylar films as BE and corresponding equivalent circuit.

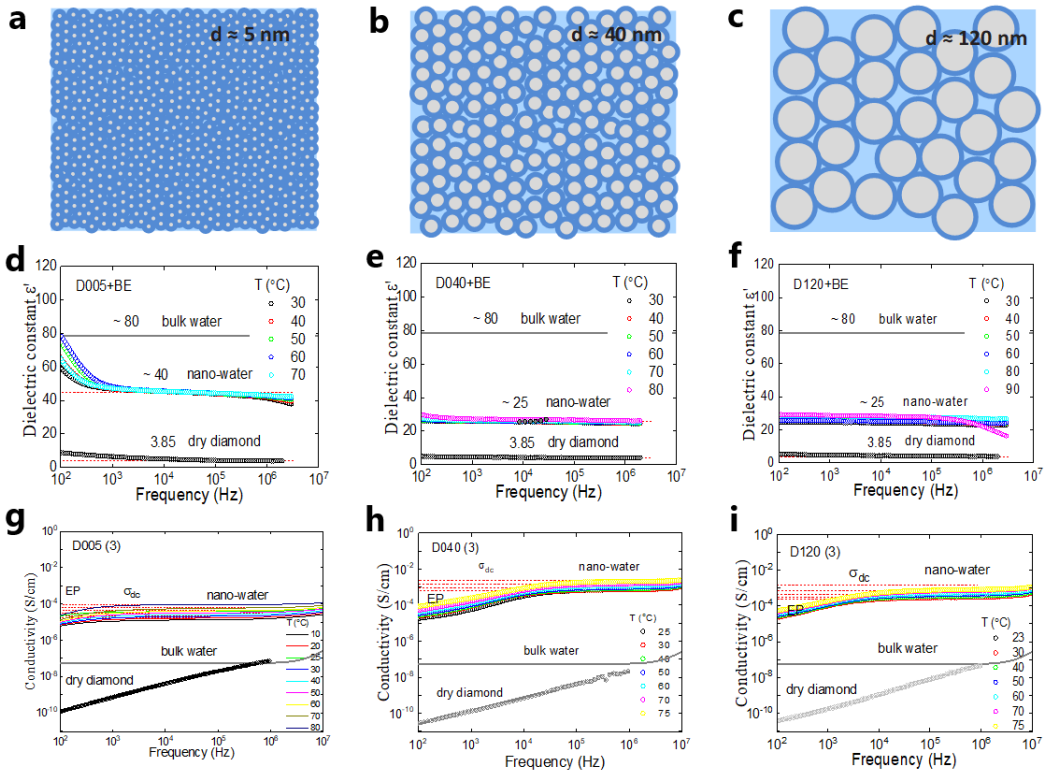

Fig. s10 | Structure and electrodynamic parameters of diamond-water effective media. **a** to **c,** model structures showing decrease of the relative volume of the interfacial water (deep blue) with grain size increase in comparison with the volumes of diamond (gray) and bulk water (light blue). **d** to **f**, and **g** to **i**, Spectra of dielectric permittivity ε' and dynamic conductivity $\sigma=\varepsilon''\varepsilon_0\omega$ of water-diamond systems in the frequency and temperature ranges from 100 Hz to 10 MHz and 298 to 348 K in comparison with the bulk water (gray lines) and dry diamond matrix (gray circles). EP is electrode polarization. Dashed red lines are guide for the eyes.

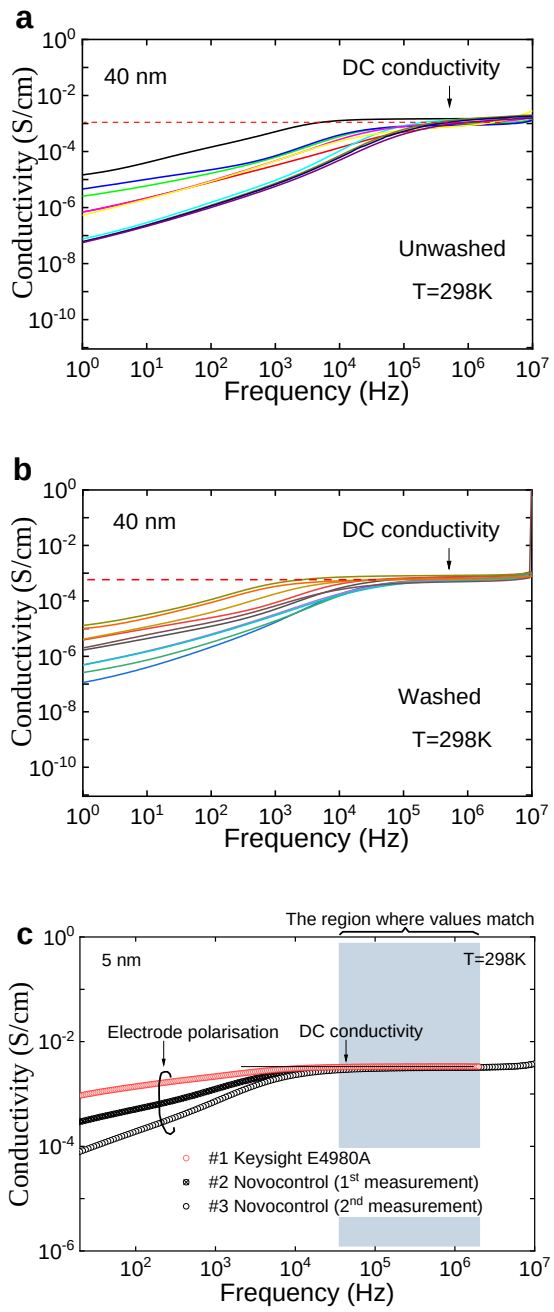

Fig. s11 | Data reproducibility. Dynamic conductivity $\sigma=\varepsilon''\varepsilon_0\omega$ at room temperature: **a**, **b** different water-diamond pellets formed from unwashed and washed powders; **c**, different devices and diamond pellet dimensions (see legend). A low frequency part affected by the electrode polarization varies significantly, but spectra coincide at the high frequency limit, where the conductivity DC was taken. Lines are guide for the eyes

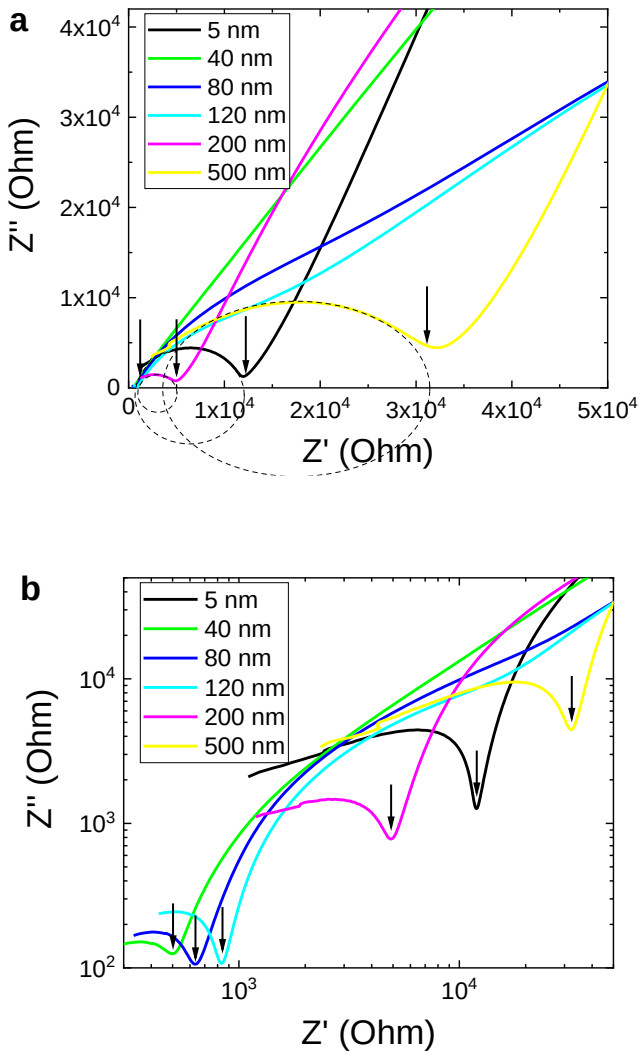

Fig. s12. Imaginary part Z'' vs. real part Z' of impedance (Nyquist plots) of ND pellets filled with water. a, Linear scale. **b**, Double-logarithmic scale. All spectra are shown at room temperature.

References

46. P. W. J. Glover and E. Walker, Grain-size to effective pore-size transformation derived from electrokinetic theory, *Geophysics*. **74,** E17–E29 (2009).

47. Sinha, Puneet K.; Wang, Chao-Yang, Pore-network modeling of liquid water transport in gas diffusion layer of a polymer electrolyte fuel cell, Electrochemica Acta 52 (28) 7936-7945 (2007)

48. O.A. Shenderova and D.M. Gruen, Ultrananocrystalline Diamond. William Andrew Publishing, Norwich, New York. 2006.

49. P. Lunkenheimer, A. Loidl, Dielectric spectroscopy of glass-forming materials: α-relaxation and excess wing. *Chemical Physics* **284**, 205-219 (2002).

50. M. Samet, V. Levchenko, G. Boiteux, G. Seytre, A. Kallel, and A. Serghei, Electrode polarization vs. Maxwell-Wagner-Sillars interfacial polarization in dielectric spectra of materials: Characteristic frequencies and scaling laws, *The Journal of Chemical Physics.* **142**, 194703 (2015).

51. Kay, Andreas; Cesar, Ilkay; Graetzel, Michael, New benchmark for water photooxidation by nanostructured alpha-Fe2O3 films. *J. Am. Chem. Soc.* **128**, 15714-15721 (2006).

52. A.A. Volkov, V.G. Artemov and A.V. Pronin, A Radically New Suggestion about the Electrodynamics of Water: Can the pH Index and the Debye Relaxation be of a Common Origin? *Eur. Phys. Lett.* **106**, 46004-6 (2014).

53. C. Bai, J. Herzfeld, Special Pairs Are Decisive in the Autoionization and Recombination of Water, *J. Phys. Chem. B.* **121**, 4213−4219 (2017).

54. G. Charron, D. Hühn, A. Perrier, L. Cordier, C. J. Pickett, T. Nann, W. J. Parak, On the Use of pH Titration to Quantitatively Characterize Colloidal Nanoparticles. *Langmuir* **28**, 15141-15149 (2012).